

High temperature thermal stability of ultrafine-grained silver processed by equal-channel angular pressing

Zoltán Hegedűs · Jenő Gubicza · Megumi Kawasaki ·
Nguyen Q. Chinh · Károly Süvegh ·
Zsolt Fogarassy · Terence G. Langdon

Received: 3 September 2012 / Accepted: 27 September 2012 / Published online: 9 October 2012
© Springer Science+Business Media New York 2012

Abstract The high temperature thermal stability of the ultrafine-grained (UFG) microstructures in low stacking-fault-energy silver was studied by differential scanning calorimetry (DSC). The UFG microstructures in two samples having purity levels of 99.995 and 99.99 at.% were achieved by four passes of equal-channel angular pressing at room temperature. The defect structure was studied by electron microscopy, X-ray line profile analysis, and positron annihilation spectroscopy before and after the exothermic DSC peak related to recovery and recrystallization. The heat released in the DSC peak was correlated to the change of defect structure during annealing. It was found

for both compositions that a considerable fraction of stored energy ($\sim 15\text{--}20\%$) was retained in the samples even after the DSC peak due to the remaining UFG regions and a large density of small dislocation loops in the recrystallized volumes. The larger impurity level in Ag yielded a higher temperature of recrystallization and a lower released heat. The latter observation is explained by the much lower vacancy concentration before the DSC peak which is attributed to the segregation of dopants at grain boundaries resulting in a smaller free volume in the interfaces.

Introduction

Bulk ultrafine-grained (UFG) metals, free of contamination, and porosity, can be processed by different ways using severe plastic deformation (SPD), such as equal-channel angular pressing (ECAP) or high-pressure torsion (HPT) [1–4]. The stability of these UFG structures is an important factor in determining their future use.

The high temperature thermal stability of pure UFG face-centered cubic (fcc) metals with medium or high stacking fault-energy (SFE) has been studied extensively by differential scanning calorimetry (DSC) [5–7]. It was found that an exothermic peak evolved during heating at a temperature of about $0.3\text{--}0.4 \times T_m$, where T_m is the absolute melting point [8, 9]. In the temperature range corresponding to the exothermic peak, both recovery (annihilation of vacancies and dislocations) and recrystallization occurred [10, 11]. For UFG fcc metals the activation energy of recovery/recrystallization is about $0.5 \pm 0.1 \times Q_{\text{self}}$, where Q_{self} is the activation energy of self-diffusion, irrespective of the SPD processing method [7, 8, 12–18]. Earlier studies showed that the activation energy of diffusion along grain boundaries and dislocations

Z. Hegedűs · J. Gubicza (✉) · N. Q. Chinh
Department of Materials Physics, Eötvös Loránd University,
Pázmány Péter s. 1/A, Budapest 1117, Hungary
e-mail: gubicza@metal.elte.hu

M. Kawasaki · T. G. Langdon
Departments of Aerospace & Mechanical Engineering
and Materials Science, University of Southern California,
Los Angeles, CA 90089-1453, USA

M. Kawasaki
Division of Materials Science and Engineering,
Hanyang University, 17 Haengdang-dong, Seongdong-gu,
Seoul 133-791, South Korea

K. Süvegh
Laboratory of Nuclear Chemistry, Eötvös Loránd University,
Pázmány Péter s. 1/A, Budapest 1117, Hungary

Z. Fogarassy
Research Institute for Technical Physics and Materials Science,
Budapest, P.O. Box 49, 1525, Hungary

T. G. Langdon
Materials Research Group, Faculty of Engineering
and the Environment, University of Southampton,
Southampton, SO17 1BJ, UK

is also about one-half of the activation energy for self-diffusion [19–21].

Experiments on 99.998 and 99.99 % purity Ni samples processed by HPT at room temperature (RT) revealed the occurrence of two exothermic peaks in the DSC thermograms [22, 23]. The smaller first peak appearing at a lower temperature corresponded to the disappearance of excess monovacancies while the larger second peak was associated with the annihilation of vacancy clusters and dislocations as well as recrystallization. The first peak was not observed for 99.99 % Cu HPT-processed under the same conditions since probably all vacancies were clustered [22]. In the case of Ni, the high values of SFE and melting point retarded the clustering of vacancies at RT because the formation of clusters on {111} planes is accompanied by the development of stacking faults and the higher melting point is associated with a larger activation energy for diffusion thereby giving a slower vacancy migration at RT.

It is apparent from the DSC results on HPT-processed Ni [22] that the value of SFE significantly influences the thermal stability of UFG fcc metals. Additional evidence for this effect is the so-called self-annealing phenomenon in low or medium SFE Ag, Au, and Cu samples when a UFG microstructure tends to recover/recrystallize during storage at RT [24–28]. Although the self-annealing phenomenon at RT in Ag with an extremely low SFE was examined earlier [27, 28], there are no reports on the high temperature stability of the UFG microstructure in SPD-processed silver.

Accordingly, experiments were conducted to investigate by DSC the high temperature thermal stability of UFG silver processed by four passes of ECAP. The evolution of the defect structure during annealing was studied by X-ray line-profile analysis (XLPA), transmission electron microscopy (TEM), and positron annihilation spectroscopy (PAS). In order to reveal the effect of impurities on the thermal stability of UFG silver, investigations were conducted on Ag samples of two different purities processed under the same conditions of ECAP.

Experimental materials and procedures

Samples of 4N5 (99.995 at.%) and 4N (99.99 at.%) purity silver were manufactured by ESPI Metals and American Elements, respectively. The alloying elements and their concentrations are listed in Table 1. For each composition, a billet with a length of ~ 70 mm and diameter of 10 mm was annealed at 741 K (corresponding to $0.6 \times T_m$) for 1 h. The annealed samples were processed through four passes of ECAP at RT with a pressing speed of ~ 8 mm/s. The pressing was conducted using route B_c where the billet is rotated in the same sense by 90° about its longitudinal axis

Table 1 The chemical composition of 4N and 4N5 purity samples: the concentration values supplied by the manufacturers are given in ppm

4N5	Cu	Pb	Fe	Se	Ir	Au	Pd
	13	14	5	6	6	10	2
4N	Cu	Pb	Fe	Se	Sb	Bi	
	30	10	10	10	10	20	

after each pass [29]. The ECAP die had an internal channel angle of 90° and an outer arc of curvature of 20° giving an equivalent strain of ~ 1 on each pass [30].

The thermal stability at elevated temperatures was investigated in an Ar atmosphere by DSC using a Perkin Elmer (DSC2) calorimeter with a heating rate of 10 K/min. The heat released during annealing was determined as the area under the exothermic peak detected in DSC experiments. The activation energy of recovery/recrystallization was determined by the conventional Kissinger-analysis, applying heating rates of 2.5, 5, 10, 20, and 40 K/min.

The microstructure immediately after ECAP as well as before and after the exothermic DSC peak was examined by XLPA on transverse sections cut perpendicular to the axes of the billets. The measurements of the X-ray diffraction lines were performed using a special high-resolution diffractometer (Nonius FR591) with $\text{CuK}\alpha_1$ radiation ($\lambda = 0.15406$ nm). The line profiles were evaluated using the convolutional multiple whole profile (CMWP) fitting procedure [31, 32]. In this method, the diffraction pattern is fitted by the sum of a background spline and the convolution of the instrumental pattern and the theoretical line profiles related to the crystallite size, dislocations, and twin faults. This procedure gives the dislocation density and the twin-boundary frequency with good statistics, where the twin-boundary frequency is defined as the fraction of twin faults among the {111} lattice planes.

The microstructures of the ECAP-processed samples and the specimens annealed up to the end of the exothermic DSC peak were examined by TEM using a Philips CM-20 microscope operating at 200 kV. The TEM samples were mechanically thinned to ~ 80 μm , cooled to liquid nitrogen temperature and then thinned with 6 keV Ar^+ ions from both sides until perforation. Finally, a thin damaged layer was removed using 2 keV Ar^+ ions. The grain structure after the DSC heat treatment was studied by electron backscatter diffraction (EBSD) using a FEI Quanta 3D scanning electron microscope.

The evolution of the vacancy concentration during annealing was studied by PAS using a ^{22}Na positron source with an activity of $\sim 10^5$ Bq covered by two Kapton foils with a thickness of 14 μm . The spectra were detected by a fast-fast spectrometer with a time resolution of ~ 205 ps and a channel time of about 10 ps. About 1.5×10^6 counts

were collected in each positron lifetime spectrum and this was fitted by the sum of three exponential components using the software RESOLUTION [33]. One of these components corresponds to the positrons annihilated in the source with fixed lifetime (390 ps) and intensity (14 %). The second component arose from positrons annihilated in the bulk crystal with a lifetime between 92 and 110 ps [34, 35], while the third component corresponds to positrons trapped and annihilated at lattice defects such as vacancies and vacancy agglomerates. The concentration (c_V) of these defects were calculated from the positron lifetime data applying the two-state simple trapping model with the specific trapping rate of $23 \pm 2 \times 10^{13} \text{ s}^{-1}$ [36].

Experimental results

Microstructure after processing by ECAP

Bright-field TEM images taken after the ECAP process are shown in Fig. 1a, b for 4N5 and 4N purity Ag samples, respectively. The grain sizes determined by TEM were close to $\sim 200 \text{ nm}$ for both samples. The dislocation density and the twin-boundary frequency values determined by XLPAs for 4N5 and 4N purity specimens were $37 \pm 4 \times 10^{14}$ and $41 \pm 5 \times 10^{14} \text{ m}^{-2}$ for the two materials and 0.7 ± 0.1 and $0.8 \pm 0.1 \%$, respectively. It is noted that both the dislocation density and the twin-boundary frequency values are exceptionally high compared to other pure fcc metals processed by ECAP [37]. This is due to the limited annihilation of the highly dissociated dislocations and the easy twinning in Ag due to the low SFE ($16\text{--}22 \text{ mJ/m}^2$ [38, 39]).

Thermal stability of the UFG microstructure

DSC measurements

Figure 2 shows DSC thermograms taken at a heating rate of 10 K/min for the ECAP-processed Ag samples. For each composition, a single exothermic peak evolved which corresponds to the recovery and recrystallization of the UFG microstructure as proven by the EBSD and XLPAs investigations presented in the following sections. There is a significant difference between the thermal stabilities of the 4N5 and 4N purity specimens as observed from the positions of the DSC peaks. Specifically, the maxima of the exothermic peaks for the 4N5 and 4N samples appear at 408 and 421 K, respectively. The higher stability of the less pure sample is attributed to the pinning effect of the impurity atoms on lattice defects (dislocations and grain boundaries).

The activation energy of recovery/recrystallization was determined from the shift of the DSC peak maximum due to a change in the heating rate using the Kissinger equation [40]:

$$\ln \frac{\beta}{T_p^2} = -\frac{Q}{k T_p} + A, \quad (1)$$

where β is the heating rate, T_p is the peak temperature, Q is the activation energy, k is the Boltzmann constant, and A is a constant. The Kissinger plots based on Eq. (1) gave 0.87 ± 0.04 and $0.96 \pm 0.05 \text{ eV}$ for the activation energies of recovery/recrystallization in 4N5 and 4N purity specimens, respectively. These values are about one-half of the activation energy of self-diffusion in Ag (1.76 eV [41]) and thus they are similar to other fcc metals processed by SPD [7, 8, 12–15, 17, 18, 23]. As the activation energy of

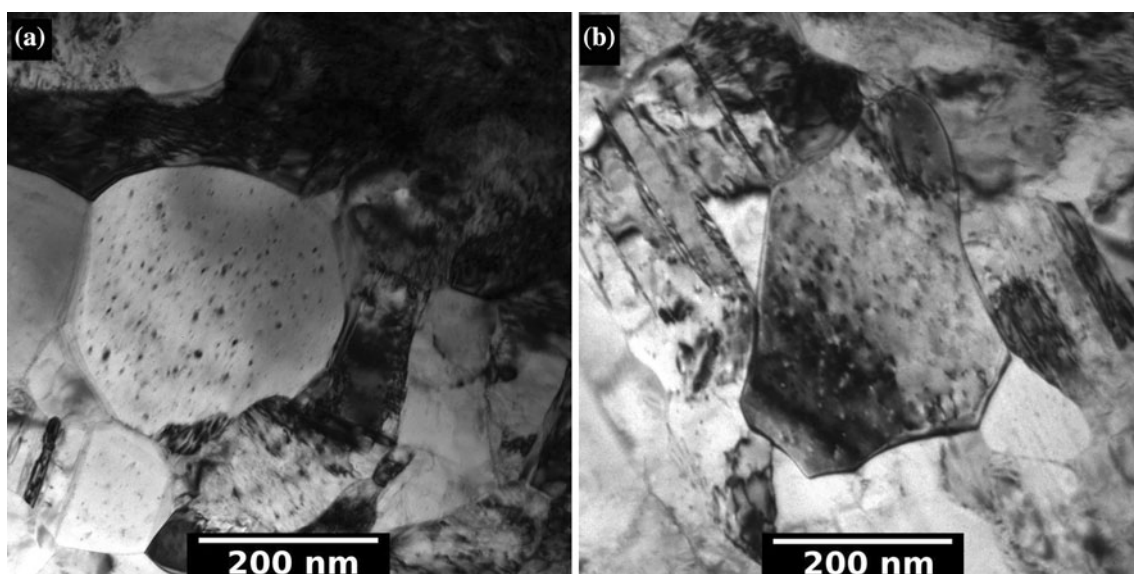


Fig. 1 Bright-field TEM images showing the microstructures immediately after ECAP-processing for **a** the 4N5 and **b** the 4N purity samples

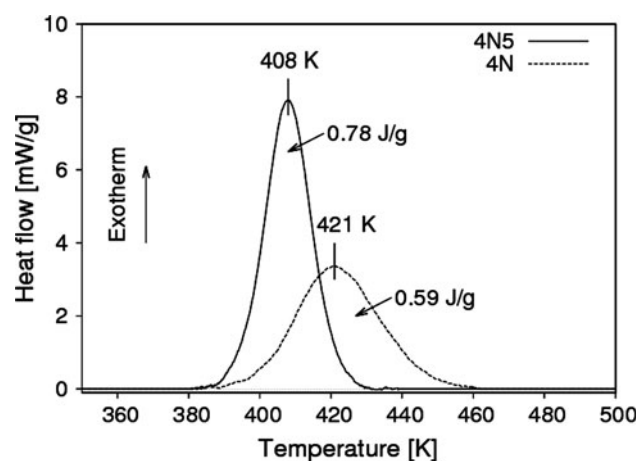


Fig. 2 DSC thermograms obtained at a heating rate of 10 K/min for the 4N5 and the 4N purity Ag samples. The values at the exothermic peaks represent the released heat

diffusion along grain boundaries and dislocations is also about one-half of the value for self-diffusion [19–21], therefore the observed values of activation energy of recovery/recrystallization in UFG materials can be explained by the large density of dislocations and grain boundaries acting as diffusion paths during annealing.

The activation energies determined in this study are very close to the values obtained earlier for Ag deformed at smaller strains [42, 43]. It is apparent from Fig. 2 that not only the temperature of the peak maximum but also the shape of the DSC peak is significantly affected by the impurity content. For the 4N purity sample, the maximum heat flow is smaller and the peak is wider than for the 4N5 purity specimen. In addition, the heat released in the DSC peak is significantly smaller for the 4N purity sample (0.59 ± 0.04 J/g) than for the 4N5 specimen (0.78 ± 0.05 J/g). In order to reveal the origin of the difference in the released heat, a detailed study of the microstructures was undertaken after the DSC peaks for both impurity levels.

EBSD study of microstructure after DSC peak

Figure 3 shows EBSD images and image quality (IQ) maps taken on 4N5 and 4N samples annealed up to the end of the exothermic DSC peak. Most of the grains are larger than several microns and have straight boundaries as in recrystallized volumes. However, some remaining UFG regions with an average grain size of ~ 300 – 700 nm are visible for both purity levels as indicated by the white arrows in Fig. 3b, d. From a comparison of several IQ maps obtained for the two impurity concentrations, the fraction of these UFG regions was slightly larger in the 4N purity sample (17 %) than in the 4N5 specimen (10 %) and this can be attributed to the pinning effect of impurities on the grain boundaries during recrystallization.

The misorientation angle distribution after the DSC peak was determined from the EBSD images and plotted in Fig. 4. For both annealed samples, the angle of misorientation is 60° for the majority of boundaries which indicate that they are $\Sigma 3$ coincidence site lattice (CSL) boundaries, i.e., the ratio of coincidence lattice points to the total number of sites is one-third in two grains separated by these boundaries. These boundaries are most probably coherent twin boundaries formed during recrystallization. The fraction of low-angle grain boundaries with angles of misorientation below 15° was larger for the 4N purity specimen (12 %) than for the 4N5 sample (7.3 %). This difference is associated with the slightly larger UFG fraction in the less pure material since boundaries with small misorientations were found in these regions.

XLPA investigation of microstructure before and after DSC peak

XLPA investigations were also carried out just before and after the DSC peak. It was found that during annealing up to the beginning of the exothermic peak the dislocation density decreased only by ~ 10 – 20 % from $37 \pm 4 \times 10^{14}$ and $41 \pm 5 \times 10^{14}$ to $32 \pm 4 \times 10^{14} \text{ m}^{-2}$ for 4N5 and 4N samples, respectively. After the DSC peak, the values of both the dislocation density and the twin-boundary frequency were lower than the detection limits of XLPA (10^{13} m^{-2} and 0.05 %, respectively), indicating that for both impurity levels the majority of dislocations were annihilated in the temperature range corresponding to the DSC peak. It is noted that if dislocation loops having a size of several nanometers remain in the microstructure after recovery/recrystallization, they are also invisible by XLPA due to their strongly shielded strain fields. The smaller released heat for the 4N purity sample is partly attributed to the larger remaining UFG fraction after the DSC peak but it may be due also to the higher concentration of vacancies, vacancy clusters or small dislocation loops remaining in the recrystallized grains due to the pinning effect of impurities. These defects are undetectable by either EBSD or XLPA and require additional studies by TEM and PAS.

TEM study of defect structure after DSC peak

Figures 5a, b shows TEM images of the interiors of recrystallized grains in 4N5 and 4N purity samples annealed up to the end of the DSC peak. Careful inspection of the images using the extinction rule for dislocations showed that the dark spots are dislocation loops having Burgers vectors of $1/2\langle 110 \rangle$ or $1/3\langle 111 \rangle$. The numbers of the investigated loops in the 4N5 and 4N purity specimens were 51 and 101, respectively. In 4N5 purity Ag, the relative fractions of dislocations with Burgers vectors of $1/2\langle 110 \rangle$ and $1/3\langle 111 \rangle$ were 81 and 19 %, respectively,

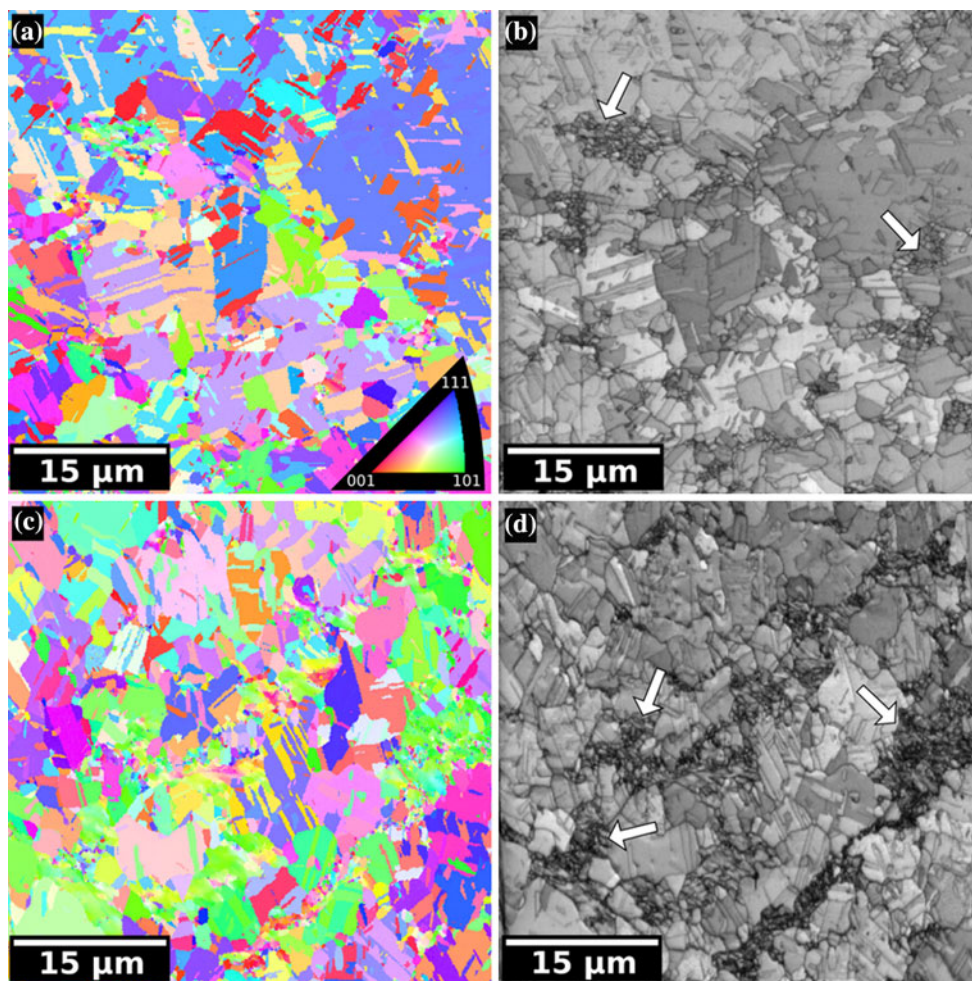


Fig. 3 EBSD images showing the orientation distributions of grains in **a** the 4N5 and **c** the 4N purity samples annealed in DSC up to the end of the exothermic peak. The image quality pictures for the same

areas show the grain boundaries in **b** the 4N5 and **d** the 4N purity samples. The remaining UFG regions are indicated by *white arrows*

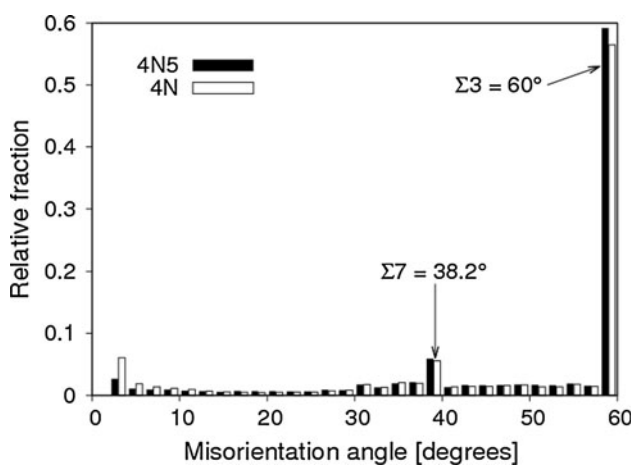


Fig. 4 Grain-boundary misorientation distributions for 4N5 and 4N purity samples ECAP-processed and then annealed in DSC up to the end of the exothermic peak. The peaks corresponding to $\Sigma 7$ and $\Sigma 3$ boundaries in the *histogram* are indicated

and for 4N purity these fractions were 72 and 28 %, respectively. Dislocations with Burgers vectors of $1/3\langle 111 \rangle$ are sessile Frank-loops which bound 2D vacancy agglomerates on $\{111\}$ planes. Clustering of vacancies into 2D configurations on $\{111\}$ planes is energetically more favorable in Ag than in other fcc metals due to the low SFE [38, 39]. The diameters of the dislocation loops are between 3 and 14 nm (the average diameter is ~ 7 nm), irrespective of their Burgers vectors and the purity level. The volume density of the dislocation loops was about $8 \pm 2 \times 10^{22} \text{ m}^{-3}$ for both impurity concentrations.

The present TEM observations reveal that after the DSC peak a considerable number of dislocation loops remain in the material even in the recrystallized volumes. It is noted that dark spots are also observed inside the grains immediately after ECAP (see Fig. 1a, b). These spots probably also correspond to dislocation loops which are formed during four passes of ECAP. However, an evaluation of

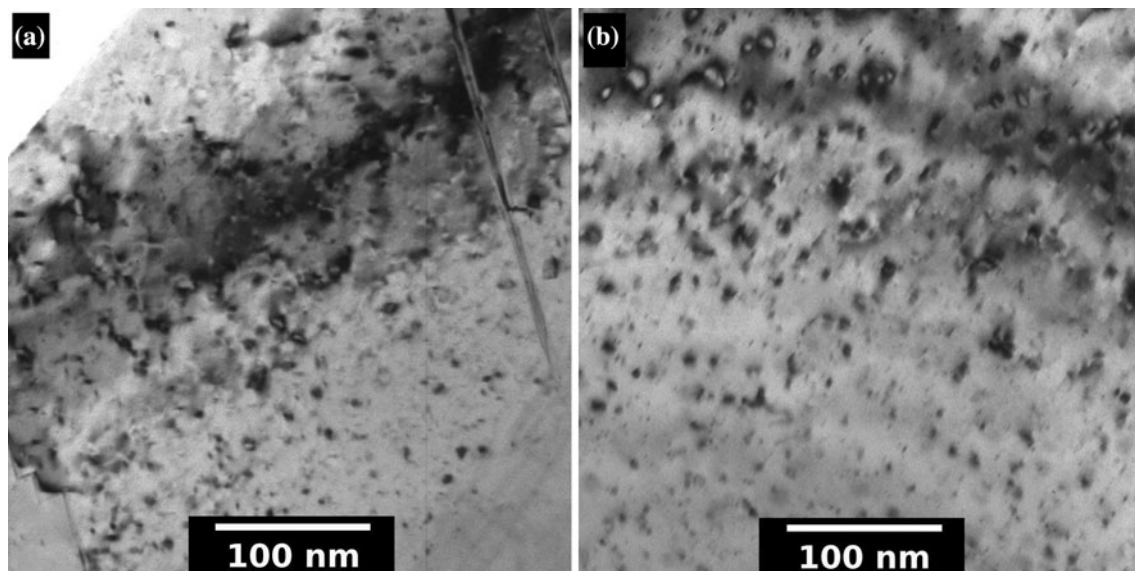


Fig. 5 TEM images showing the recrystallized microstructures for **a** the 4N5 and **b** the 4N purity samples after heat treatment in DSC up to the end of the exothermic peak

these types of loops in the TEM images was unsuccessful due to the highly distorted microstructures. The density of loops after ECAP was similar to the density after the DSC peak but their size was slightly smaller.

PAS investigation of defects before and after DSC peak

The change of vacancy concentration during the evolution of the exothermic DSC peak was investigated by PAS. The experimental lifetimes of positrons annihilated at defects in both 4N5 and 4N purity samples before and after the DSC peak are between 181 and 201 ps. These values are close to the positron lifetime of monovacancies in plastically deformed Ag (196 ps, [34]). However, even at the beginning of the exothermic peak, at ~ 380 K, the temperature is too high for monovacancies to exist. If the vacancies agglomerate into 3D clusters, the positron lifetime would be much higher than the value for a monovacancy. The absence of 3D vacancy agglomerates can be attributed to the low SFE of Ag because, even if they formed, their collapse into 2D clusters is energetically favorable [44].

In Ag, the 2D vacancy clusters usually form on $\{111\}$ planes and these agglomerates may be regarded as a stacking fault bordered by a Frank dislocation loop with a Burgers vector of $1/3\langle 111 \rangle$. The lifetime of positrons annihilated at these 2D clusters is only slightly smaller than the value for monovacancies [45, 46]. The positron lifetime for free volumes of approximately the size of a monovacancy in the grain boundaries is also close to the value characteristic for monovacancies [47]. Therefore, it is expected that the concentration obtained by PAS describes vacancies in 2D collapsed clusters and grain boundaries.

At the beginning of the exothermic peak, at ~ 380 K, the vacancy concentration in 4N5 purity sample was larger than the detection limit in the PAS experiments ($\sim 5 \times 10^{-5}$) while for the 4N specimen the value was determined as $0.8 \pm 0.1 \times 10^{-5}$. The considerably smaller vacancy concentration in the 4N sample compared to the 4N5 specimen can be explained by the segregation of impurity atoms at the grain interfaces which make small free volumes in the boundaries invisible for positrons.

During the evolution of the DSC peak, the vacancy concentration decreased from a value higher than 5×10^{-5} to $0.7 \pm 0.1 \times 10^{-5}$ in the 4N5 specimen while in the 4N sample the vacancy concentration increased from $0.8 \pm 0.1 \times 10^{-5}$ to $1.5 \pm 0.1 \times 10^{-5}$. This increase in vacancy concentration is due to the release of the free volumes in the grain boundaries into the lattice in the form of vacancies during recrystallization [48–50]. Therefore, the former small interface free volumes became detectable for positrons, resulting in an increase in the measured vacancy concentration. Similar vacancy production most probably also occurs in the 4N5 purity sample but all of these vacancies were annihilated before the end of the DSC peak. At the same time, in the 4N specimen a fraction of the vacancies formed during recrystallization was trapped in the microstructure due to the pinning effect of large impurities (Pb, Sb, and Bi) as in earlier observation [51].

Discussion

It is important to compare the values for the released heat for the 4N5 and 4N purity samples with the difference

Table 2 The balance table for stored energies calculated for the different lattice defects in 4N5 and 4N purity samples before and after the DSC peak

	4N5			4N		
	Before the DSC peak	After the DSC peak	Difference	Before the DSC peak	After the DSC peak	Difference
E_{disl} (J/g)	0.28	0–0.02	0.26–0.28	0.28	0–0.04	0.24–0.28
E_{HAGB} (J/g)	0.36	0.01	0.35	0.36	0.02	0.34
E_{twin} (J/g)	0.02	0	0.02	0.02	0	0.02
E_{loop} (J/g)	0.09	0.09	0	0.09	0.09	0
E_{vac} (J/g)	≥0.05	0.01	≥0.04	0.01	0.01	0
Sum (J/g)	≥0.80	0.11–0.13	≥0.67–0.69	0.76	0.12–0.16	0.60–0.64
Experimental (J/g)			0.78			0.59

The difference between the stored energies determined before and after the peak is used to estimate the contributions of the various lattice defects to the heat released in the exothermic DSC peak. E_{disl} , dislocations; E_{HAGB} , high-angle grain boundaries; E_{twin} , twin boundaries; E_{loop} , small dislocation loops; E_{vac} , vacancies

between the stored energies calculated before and after the DSC peak. The stored energy per unit mass in the two ECAP-processed UFG Ag samples before and after the DSC peak is determined as the sum of the energies of the lattice defects (grain boundaries, dislocations, twin faults, small dislocation loops, and vacancies) investigated in the previous sections. It is noted that the values of the calculated energies in this report are rounded to the precision of the measured released heat which corresponds to two decimal places.

The energy stored in dislocations (E_{disl}) can be determined from the dislocation density using the following relationship [37]:

$$E_{\text{disl}} = A \frac{Gb^2\rho}{\rho_m} \ln \frac{1}{b\sqrt{\rho}}, \tag{2}$$

where G is the shear modulus (30 GPa), b is the magnitude of Burgers vector (0.29 nm), ρ is the dislocation density, and A denotes a factor which depends on the edge/screw character of the dislocations. The value of A is equal to $(4\pi)^{-1}$ and $(4\pi(1-\nu))^{-1}$ for screw and edge dislocations, respectively, where ν is Poisson’s ratio (taken as 0.3).

The parameter q determined from X-ray line-profile analysis describes the edge/screw character of the dislocations. The theoretically calculated values of q for pure edge and screw dislocations in Ag are 1.62 and 2.35, respectively. In practice, the value of A was obtained from the experimentally determined q of 2.2 using a simple rule of mixtures [9]:

$$A = \frac{q - 1.62}{0.73} \frac{1}{4\pi} + \frac{2.35 - q}{0.73} \frac{1}{4\pi(1-\nu)}. \tag{3}$$

The energy stored in dislocations calculated from the dislocation density determined by XLPA is 0.28 J/g for both samples before the DSC peak. After this peak in the recrystallized region, the dislocation density was smaller

than the detection limit of XLPA (10^{13} m^{-2}) which is two orders of magnitude lower than the value determined before the DSC peak. Therefore, this contribution to the stored energy may be neglected. In the remaining UFG region, the dislocation density is most probably higher than the detection limit but its value is not easily determined by XLPA due to the relatively small volume fraction of this region. Therefore, an upper limit of E_{disl} in the remaining UFG region was calculated as the product of the dislocation density before the DSC peak and the fraction of the UFG volumes: thus, 0.02 and 0.04 J/g were obtained for the 4N5 and 4N purity samples, respectively. The calculated values of the stored energy are summarized in Table 2.

The interfaces between the grains can be classified as low- and high-angle grain boundaries (LAGBs and HAGBs, respectively). The LAGBs usually consist of dislocations and XLPA measures dislocations in both the boundaries and the interiors of the grains so that the contribution of LAGBs to the stored energy is incorporated in Eq. (2). The energy of the HAGBs (E_{HAGB}) is given as [52]:

$$E_{\text{HAGB}} = h \frac{3\gamma_{\text{GB}}}{d\rho_m}, \tag{4}$$

where γ_{GB} is the average HAGB energy in Ag (0.5 J/m² [53]), h is the fraction of HAGBs (about 0.5 for fcc metals processed by four passes of ECAP [54]), d is the average grain size and ρ_m is the mass density ($10.5 \times 10^6 \text{ g m}^{-3}$). Before the DSC peak, the average grain size in both samples is 200 nm which gives 0.36 J/g for the grain boundary energy. It is noted that in the less pure material the segregation of large atoms to grain boundaries reduces the grain boundary energy [55]. However, taking into account the total concentration of large dopants in 4N purity sample ($c_d = 4 \times 10^{-5}$ for Pb, Sb, and Bi), the

reduction in grain boundary energy is negligibly small at about 2 % [55]. After the DSC peak, the microstructure for both purity levels consists of recrystallized coarse-grains and the remaining UFG regions with average grain sizes of 5 μm and 500 nm, respectively. The energy stored in HAGBs in the recrystallized fraction is negligible since, as shown in Fig. 4, most are twin boundaries having very low energy (0.008 J/m² [38]). Taking into account the relative fraction of the remaining UFG regions, the energies stored in the HAGBs after the DSC peak are ~ 0.01 and ~ 0.02 J/g for the 4N5 and 4N purity samples, respectively.

The stored energy for twin faults (E_{twin}) in cubic grains can be calculated as:

$$E_{\text{twin}} = \gamma_{\text{twin}} d^2 \frac{d}{d_{\text{twin}} d^3 \rho_{\text{m}}} = \frac{\gamma_{\text{twin}} \beta}{d_{111} \rho_{\text{m}}}, \quad (5)$$

where γ_{twin} is the twin-boundary energy in Ag, β is the twin-boundary frequency determined by XLPAs (0.7 ± 0.1 % before the DSC peak for both impurity levels), d_{111} is the spacing between the neighboring {111} planes (0.24 nm) and d_{twin} is the mean twin-boundary spacing which can be expressed as d_{111}/β . The value of E_{twin} is ~ 0.02 J/g for both 4N5 and 4N specimens before the DSC peak and practically zero after the peak due to the very large mean twin-boundary spacing (>1 μm).

The stored energy for the small dislocation loops (E_{loop}) with Burgers vector of $1/2\langle 110 \rangle$ in the recrystallized fraction after the DSC peak may be expressed by modifying Eqs. (2) and (3) as:

$$E_{\text{loop}} = g \frac{1}{8\pi} \left(1 + \frac{1}{1-\nu} \right) \frac{Gb^2 f \rho_{\text{loop}}}{\rho_{\text{m}}} \ln \frac{D}{b}, \quad (6)$$

where g is the recrystallized volume fraction. The outer cut-off radius of dislocations in the loops was selected as the average diameter of the loops ($D = 7$ nm as determined by TEM) and ρ_{loop} is the total length of dislocations in the loops in a unit volume (i.e., the dislocation density in the loops with both Burgers vectors) and f is the fraction of dislocation loops with Burgers vector of $1/2\langle 110 \rangle$. The value of ρ_{loop} was determined as the product of the average length of a loop ($D\pi$) and the volume density of the dislocation loops ($r_{\text{loop}} = 8 \times 10^{22}$ m⁻³). Calculating the energies stored in the loops after the DSC peak using Eq. (6), values of ~ 0.09 J/g were obtained for both samples. As the density and the size of the dislocation loops immediately after ECAP appears to similar to the values after the DSC peak, the same stored energies were assumed for the loops both before and after the DSC peak. This means that the loops make a negligible contribution to the released heat despite their high density. The loops with Burgers vector of $1/3\langle 111 \rangle$ are practically collapsed vacancy clusters, therefore their stored energy is included

in the energy calculated from the vacancy concentration in the next paragraph.

The energy stored in the vacancies (E_{vac}) may be expressed by the measured vacancy concentration (c_{v}) as [37]:

$$E_{\text{vac}} = e_{\text{vac}} c_{\text{v}} \frac{N_{\text{A}}}{M}, \quad (7)$$

where e_{vac} is the formation energy of a vacancy (1.1 eV = 0.176×10^{-18} J [41]), N_{A} is Avogadro's number (6×10^{23} mol⁻¹) and M is the molar mass (107.87 g/mol). The values of E_{vac} were determined from the vacancy concentrations measured by PAS and listed in Table 2. It is noted that the segregation of the large dopants to vacancies with a maximum binding energy of ~ 0.3 eV [56] may reduce the vacancy energy by 30 % which is negligible by comparison with other contributions.

Summing up the stored energies calculated for the different lattice defects, the total energies stored in the 4N5 and 4N purity specimens before and after the DSC peak are listed in Table 2. These calculations show that the largest contributions to the stored energy before the DSC peak are given by dislocations and HAGBs. After the DSC peak, about 15–20 % of the stored energy is retained in the material due to the remaining UFG fraction and the dislocation loops in the recrystallized volumes. The difference between the total energies obtained before and after the DSC peak gives the calculated released heat. For the 4N purity sample the measured heat (0.59 ± 0.04 J/g) and its calculated value (0.60–0.64 J/g) agree within the experimental error. For the 4N5 purity sample only a lower bound for the released heat can be calculated since the vacancy concentration was larger than the detection limit of PAS. In this case the calculated value of the released heat is larger than 0.67–0.69 J/g which is in accordance with the experimentally measured value of 0.78 ± 0.04 J/g. Assuming an agreement between the calculated and the measured values of the heat release for the 4N5 purity specimen, the vacancy concentration before the DSC peak can be determined from Eq. (7) as $\sim 1.5 \times 10^{-4}$. This means that the much lower heat released for the 4N purity sample compared to the 4N5 purity specimen is mainly attributed to an order of magnitude smaller vacancy concentration. It is emphasized that the vacancy concentration obtained by PAS includes also the free volumes in the grain boundaries. The segregation of impurities to these boundaries reduces the measured vacancy concentration in the 4N purity sample.

It should be noted that the degree of impurity segregation to grain boundaries depends not only on the concentration but also on the type of dopants. The preference of a solute to dissolve either in an ordered crystal lattice or in a disordered grain boundary is characterized by the distribution coefficient, k [57]. For a dilute binary alloy, this

quantity is defined as the ratio of the concentrations in the solid and the liquid phases under equilibrium conditions where the liquid phase corresponds to the disordered phase. For a solute–solvent atom pair, if $k > 1$ or $k < 1$ the solute prefers either an ordered or a disordered environment, respectively. This preference depends on the ratio of the radii of the solute and solvent atoms, on the difference between their electronegativities and their valence numbers [56]. Among the impurities found in the silver materials used in this investigation, the dopants Cu, Sb, Se, Pb, and Bi have $k < 1$ [57–60]. In the 4N purity sample the concentration sum for these elements is 80 ppm and this is much higher than the concentration of 33 ppm for the 4N5 specimen although both impurity contents are very low. However, it was shown for rolled Cu–Ag alloys, where Ag solute in Cu has $k < 1$, that only 80 ppm Ag leads to a 30 % reduction in the released heat compared to Cu with a Ag concentration of 30–40 ppm [57]. The present results show a similar effect of impurities in Ag, thereby demonstrating that a very small difference in the impurity level produces a significant variation in the heat released during annealing.

Conclusions

1. Experiments were conducted to investigate the high temperature thermal stability of 4N5 (99.995 at.%) and 4N (99.99 at.%) purity silver after processing by ECAP: The results show the activation energies for recovery and recrystallization are similar for both materials but the temperature of the exothermic DSC peak maximum is higher and the heat released is lower for the 4N purity sample.
2. The primary contributions to the stored energy before recovery/recrystallization are given by the grain boundaries and dislocations. A significant fraction of stored energy (~ 15 – 20 %) was retained in the samples after the exothermic DSC peak due to the remaining UFG regions and the high density of small dislocation loops.
3. The reduced heat released for the 4N purity sample is primarily due to the lower vacancy concentration before the DSC peak compared to the 4N5 purity specimen. This phenomenon is attributed to a reduction of free volumes by segregation of dopants at the grain interfaces.

Acknowledgements This study was supported in part by the Hungarian Scientific Research Fund, OTKA, Grant No. K-81360, in part by the National Science Foundation of the United States under Grant No. DMR-0855009 (MK and TGL) and in part by the European Research Council under ERC Grant Agreement No. 267464-SPDMETALS

(TGL). The European Union and the European Social Fund have provided financial support to this project under Grant Agreement No. TÁMOP 4.2.1./B-09/1/KMR-2010-0003. The authors thank Andrea Jakab for preparation of the TEM samples and Zoltán Dankházi for evaluating the EBSD results.

References

1. Segal VM (1999) *Mater Sci Eng A* 271:322
2. Valiev RZ, Islamgaliev RK, Alexandrov IV (2000) *Prog Mater Sci* 45:103
3. Valiev RZ, Langdon TG (2006) *Prog Mater Sci* 51:881
4. Zhilyaev AP, Langdon TG (2008) *Prog Mater Sci* 53:893
5. Cao WQ, Godfrey A, Liu W, Liu Q (2003) *Mater Sci Eng A* 360:420
6. Molodova X, Gottstein G, Winning M, Hellmig RJ (2007) *Mater Sci Eng A* 460–461:204
7. Cao WQ, Gu CF, Pereloma EV, Davies CHJ (2008) *Mater Sci Eng A* 492:74
8. Zhilyaev AP, Nurislamova GV, Surinach S, Baró MD, Langdon TG (2002) *Mater Phys Mech* 5:23
9. Gubicza J, Dobatkin SV, Khosravi E, Kuznetsov AA, Lábár LJ (2011) *Mater Sci Eng A* 528:1828
10. Gubicza J, Nam NH, Balogh L, Hellmig RJ, Stolyarov VV, Estrin Y, Ungár T (2004) *J Alloys Compd* 378:248
11. Gubicza J, Balogh L, Hellmig RJ, Estrin Y, Ungár T (2005) *Mater Sci Eng A* 400–401:334
12. Huang YK, Menovsky AA, de Boer FR (1993) *Nanostruct Mater* 2:587
13. Kumpmann A, Günther B, Kunze H-D (1993) *Mater Sci Eng A* 168:165
14. Zhilyaev AP, Nurislamova GV, Valiev RZ, Baró MD, Langdon TG (2002) *Metall Mater Trans A* 33:1865
15. Cizek J, Prochazka I, Cieslar M, Kuzel R, Kuriplach J, Chmelik F, Stulikova I, Becvar F, Melikhova O (2002) *Phys Rev B* 65:094106
16. Zhilyaev AP, Gubicza J, Nurislamova G, Révész Á, Surinach S, Baró MD, Ungár T (2003) *Phys Stat Sol (A)* 198:263
17. Zhilyaev AP, Kim B-K, Szpunar JA, Baró MD, Langdon TG (2005) *Mater Sci Eng A* 391:377
18. Lugo N, Llorca N, Sunol JJ, Cabrera JM (2010) *J Mater Sci* 45:2264. doi:10.1007/s10853-009-4139-7
19. Lian J, Valiev RZ, Baudelet B (1995) *Acta Metall Mater* 43:4165
20. Tjong SC, Chen H (2004) *Mater Sci Eng, R* 45:1
21. Kuo C-M, Lin C-S (2007) *Scr Mater* 57:667
22. Setman D, Schafner E, Korznikova E, Zehetbauer MJ (2008) *Mater Sci Eng A* 493:116
23. Setman D, Kerber MB, Schafner E, Zehetbauer MJ (2010) *Metall Mater Trans A* 41:810
24. Wang G, Wu SD, Zuo L, Esling C, Wang ZG, Li GY (2003) *Mater Sci Eng A* 346:83
25. Estrin Y, Isaev NV, Lubenets SV, Malykhin SV, Pugachov AT, Pustovalov VV, Reshetnyak EN, Fomenko VS, Fomenko LS, Shumilin SE, Janecek M, Hellmig RJ (2006) *Acta Mater* 54:5581
26. Matsunaga M, Horita Z (2009) *Mater Trans* 50:1633
27. Gubicza J, Chinh NQ, Lábár LJ, Hegedűs Z, Langdon TG (2010) *Mater Sci Eng A* 527:752
28. Hegedűs Z, Gubicza J, Kawasaki M, Chinh NQ, Fogarassy Zs, Langdon TG (2011) *Mater Sci Eng A* 528:8694
29. Furukawa M, Iwahashi Y, Horita Z, Nemoto M, Langdon TG (1998) *Mater Sci Eng A* 257:328
30. Iwahashi Y, Wang J, Horita Z, Nemoto M, Langdon TG (1996) *Scr Mater* 35:143
31. Ribárik G, Gubicza J, Ungár T (2004) *Mater Sci Eng A* 387–389:343

32. Balogh L, Ribárik G, Ungár T (2006) *J Appl Phys* 100:023512
33. Kirkegaard P, Eldrup M, Mogensen OE, Pedersen NJ (1981) *Phys Commun* 23:307
34. Folegati P, Makkonen I, Ferragut R, Puska MJ (2007) *Phys Rev B* 75:054201
35. Shrivastava SB, Bonde HP (1978) *Phys Stat Sol (B)* 88:269
36. Hehenkamp Th (1994) *J Phys Chem Solids* 55:907
37. Schafner E, Steiner G, Korznikova E, Kerber M, Zehetbauer MJ (2005) *Mater Sci Eng A* 410–411:169
38. Hirth JP, Lothe J (1982) *Theory of dislocations*. Wiley, New York
39. Murr LE (1975) *Interfacial phenomena in metals and alloys*. Addison Wesley, Reading
40. Kissinger HE (1957) *Anal Chem* 29:1702
41. Balluffi RW (1978) *J Nucl Mater* 69–70:240
42. Dawson HI (1965) *Acta Metall* 13:453
43. Kamel R, Attia EA (1961) *Acta Metall* 9:1047
44. Linderoth S, Hidalgo C (1987) *Phys Rev B* 36:4054
45. Hakkinen H, Makinen S, Manninen M (1990) *Phys Rev B* 41:12441
46. Gröger V, Geringer T, Pichl W, Krexner G, Novotny I, Procházka I (1996) *Mater Sci Forum* 210–213:743
47. Schaefer H-E, Wurschum R, Birringer R, Gleiter H (1988) *Phys Rev B* 38:9545
48. Lucke K, Gottstein G (1981) *Acta Metall* 29:779
49. Estrin Y, Gottstein G, Shvindlerman LS (1999) *Acta Mater* 47:3541
50. Shvindlerman LS, Gottstein G, Ivanov VA, Molodov DA, Kolosnikov D, Lojkowski W (2006) *J Mater Sci* 41:7725. doi: [10.1007/s10853-006-0563-0](https://doi.org/10.1007/s10853-006-0563-0)
51. Wegner D (1988) *J Phys F: Met Phys* 18:2291
52. Humphreys FJ, Hatherly M (2004) *Recrystallization and related annealing phenomena*, 2nd edn. Elsevier, Oxford
53. Wolf D (1984) *Acta Metall* 32:735
54. Kawasaki M, Horita Z, Langdon TG (2009) *Mater Sci Eng A* 524:143
55. Millett PC, Selvam RP, Saxena A (2007) *Acta Mater* 55:2329
56. Klemradt U, Drittler B, Hoshino T, Zeller R, Dederichs PH, Stefanou N (1991) *Phys Rev B* 43:9487
57. Haessner F, Hoschek G, Tolg G (1979) *Acta Metall* 27:1539
58. Karakaya I, Thompson WT (1990) *J Phase Equilibria* 11:266
59. Lee B-Z, Oh C-S, Lee DN (1994) *J Alloys Compd* 215:293
60. Liu J, Guo C, Li C, Du Z (2012) *Thermochim Acta* 539:44